Design Considerations for a Steerable Needle Robot to Maximize Reachable Lung Volume

Inbar Fried[1,2], Janine Hoelscher[1], Mengyu Fu[1], Maxwell Emerson[3], Tayfun Efe Ertop[3], Margaret Rox[3], Josephine Granna[3], Alan Kuntz[4], Jason A. Akulian[5], Robert J. Webster III[3], and Ron Alterovitz[1]

***Abstract*— Steerable needles that are able to follow curvilinear trajectories and steer around anatomical obstacles are a promising solution for many interventional procedures. In the lung, these needles can be deployed from the tip of a conventional bronchoscope to reach lung lesions for diagnosis. The reach of such a device depends on several design parameters including the bronchoscope diameter, the angle of the piercing device relative to the medial axis of the airway, and the needle's minimum radius of curvature while steering. Assessing the effect of these parameters on the overall system's clinical utility is important in informing future design choices and understanding the capabilities and limitations of the system. In this paper, we analyze the effect of various settings for these three robot parameters on the percentage of the lung that the robot can reach. We combine Monte Carlo random sampling of piercing configurations with a Rapidly-exploring Random Trees based steerable needle motion planner in simulated human lung environments to asymptotically accurately estimate the volume of sites in the lung reachable by the robot. We highlight the importance of each parameter on the overall system's reachable workspace in an effort to motivate future device innovation and highlight design trade-offs.**

I. INTRODUCTION

Robotically-deployed steerable needles that are capable of following curvilinear trajectories have the potential to improve clinical outcomes in numerous applications including lung nodule biopsy [1], liver radiofrequency ablation [2], and direct therapeutic delivery to brain tumors [3]. These systems offer several advantages, including increased biopsy accuracy through real-time trajectory correction, multi-target reach from a given insertion point, and the ability to steer around anatomical obstacles to access clinical targets that are not easily accessible with traditional rigid tools.

Given the high incidence of lung cancer in the United States (over 220,000 new cases per year [4]) and the limitations of existing diagnostic tools [5], [6], developing a steerable needle system for this application could significantly improve early diagnosis and patient survival. One such previously described system consists of three components: a conventional bronchoscope for airway navigation, a piercing mechanism that exits the airway into the lung parenchyma, and a steerable needle for target biopsy [1]. Developing an understanding of how the different system components contribute to the overall reachable workspace of such a device is important in assessing their clinical utility and in informing future innovation. In this paper, we evaluate the effect of several design choices for such a bronchoscopically-deployed robotically-actuated steerable needle system on its reachable workspace. By doing so, we quantitatively evaluate the clinical accessibility capabilities of the system.

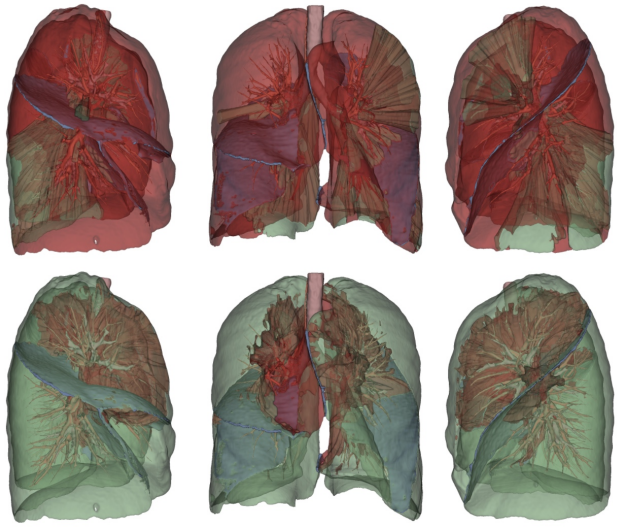

Fig. 1. A visualization of the reachable workspace (green) and unreachable regions (red) for two designs of the steerable needle robot in a human lung environment with anatomical obstacles. The top and bottom rows represent results for the most constrained design and most capable design we consider, respectively.

The reachable workspace of a robot can be described by all points in the environment that can be reached by the end effector of the robot via a collision-free motion starting from a valid start configuration. If a target falls within this workspace, then there exists some sequence of collision-free configurations of the robot that ultimately reach it. For the lung robot system, the environment we are interested in includes the lung parenchyma, which contains anatomical obstacles. Several key parameters influence the reachable workspace including the bronchoscope radius which affects the airway depth that can be accessed, the piercing angle

This research was supported by the U.S. National Institutes of Health (NIH) under award R01EB024864.

The authors acknowledge the National Cancer Institute and the Foundation for the National Institutes of Health, and their critical role in the creation of the free publicly available LIDC/IDRI Database used in this study.

[1]Department of Computer Science, University of North Carolina at Chapel Hill, Chapel Hill, NC 27599, USA. {ifried01, mfu, jhoelsch, ron}@cs.unc.edu

[2] University of North Carolina School of Medicine, Chapel Hill, NC 27599, USA.

[3] Department of Mechanical Engineering, Vanderbilt University, Nashville, TN 37235, USA.

[4]School of Computing and the Robotics Center, University of Utah, Salt Lake City, UT 84112, USA.

[5]Division of Pulmonary Diseases and Critical Care Medicine, University of North Carolina School of Medicine, Chapel Hill, NC 27514, USA.

through the airway wall into the parenchyma that determines the starting pose for needle deployment, and the minimum radius of curvature of the steerable needle which allows the needle to steer around obstacles.

There has been work done towards improving the individual system parameters mentioned above. For example, bronchoscope development has resulted in ultrathin bronchoscopes measuring just 3.0 mm in diameter [7], with several studies in cadavers showing improved lung access using these devices [8]. Likewise, extensive research efforts have developed steerable needles that can curve with lower radius of curvature, with the newest designs able to achieve a radius of curvature in gel of 60.1 mm and even lower in specific ex-vivo tissue [9], [10], [11]. However, little work has been done to quantify how characteristics of the different parameters contribute to overall lung access in a single system. Fig. 1 shows a visualization of what this reachable workspace looks like for two different system designs in a lung environment, highlighting the importance of good design choices.

In this work, we use Monte Carlo random sampling of piercing poses and a motion planning algorithm for the steerable needle inspired by the Rapidly-exploring Random Trees (RRT) algorithm [12] to characterize the clinical reachable workspace of a bronchoscopically-deployed steerable needle lung biopsy robot. We specifically analyze the contributions of three system parameters to overall lung reachability and by doing so highlight system requirements and areas for future improvement. We use motion planning to approximate the reachable workspace which guarantees that all points in the reachable space are accessible with a collision-free trajectory with relation to the surrounding anatomy (i.e., blood vessels, bronchial tree, lung fissures, lung pleura). This is critical for clinical evaluation of this device. We also use a measure of reachable redundancy to determine the robustness of system designs and lung regions to piercing variability.

To our knowledge, this is the first evaluation of the reachable workspace for a steerable needle system in human lungs.

II. Related Work

Our work to determine the effects of various parameters on the system's overall capabilities parallels work done in the space of design optimization. The concept of design optimization for medical robots has been applied to various systems, including surgical robotic arm carriers [13], ankle rehabilitation systems [14], [15], surgical tool manipulators [16], [17], novel surgical robots [18], exoskeletons [19], and soft robots [20], to name a few. Kuo et al. [21] published a meta-analysis of design considerations for minimally invasive surgical robots.

Concentric tube continuum robots, a class of surgical robots, have received significant attention in design optimization because of their many design parameters [22]. Many of the related works have considered design with respect to anatomically defined environmental constraints [23], [24], [25], [26], including lung environments [27], [28]. The approaches across these papers include geometric

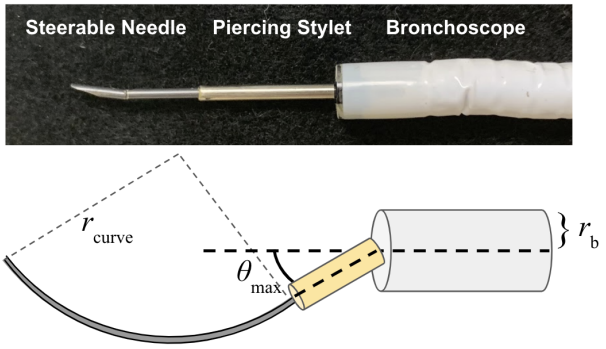

Fig. 2. The three components of the robot along with the design parameters considered in this paper.

approaches, genetic algorithms, simulated annealing [29], and even human-in-the-loop approaches [30].

Several works on design optimization leverage motion planning because it allows for accurate consideration of obstacles in the workspace throughout the entire robot deployment [18], [23], [27]. For this reason, we also use motion planning in our analysis. There has been substantial work regarding motion planning for steerable needles [31], [32], [33], including approaches that consider optimization [34], inverse-kinematics [35], replanning during needle deployment [36], [37], [38], and uncertainty in the motion [39], [40]. Xu et al. were the first to introduce an RRT-based motion planner for needle steering [41]. Kuntz et al. introduced an RRT-based motion planner for a three-stage lung robot system with a steerable needle [42]. More recently, Pinzi et al. introduced an algorithm for needle steering based off of the Adaptive Fractal Tree algorithm [43] and optimized geometric Hermite curves that incorporates heading constraints for both the start and goal poses [44]. The motion planner used in this work builds off of the approach introduced in Patil et al. [45].

Evaluating the workspace of a robot can help describe the capabilities of a system or evaluate design choices [28], [46]. Burgner-Kahrs et al. characterize the reachable workspace of a concentric tube robot in free space without considering any specific environment or obstacles [47]. They use Monte Carlo sampling to capture a comprehensive distribution of the joint space inspired by prior work [48]. Adebar et al. evaluated the reachable workspace of a steerable needle system for radiofrequency ablation in a simulated human liver model. They concluded that 50mm minimum radius of curvature needles would be sufficient for the specific operation, and argued for future innovation towards this goal [11]. Inspired by this work, we characterize the reachable workspace for a steerable-needle robot in simulated human lungs with real anatomical obstacles. We parameterize the system by three parameters and consider each of their effects on the system's reachable workspace.

III. Problem Definition

The bronchoscopically-deployed steerable needle system we consider here is composed of three components: a bronchoscope, a piercing mechanism, and a steerable needle

(as shown in Fig. 2). We capture the space in which the system operates by segmenting the anatomy from a preoperative CT scan. The CT scan is represented as a three-dimensional array consisting of voxels of fixed size. The segmentation process can be done automatically or manually, and the resulting segmented anatomy is represented as three-dimensional arrays of the same size as the original CT scan with voxel coordinates indicating the presence or absence of the segmented anatomy in the space. We define the set of obstacles $O \in \mathbb{R}^3$ by the union of all voxels that make up major blood vessels, airways, lung fissures separating lung lobes, and the space outside of the pleural boundary in the segmentation arrays.

A. Design Space

We model the bronchoscope by its axial cross-sectional radius r_{b}, which determines the depth it can reach in the airways. The piercing mechanism is modeled as a straight stylet with a fixed length l_s and a maximum achievable exit angle relative to the medial axis of the airway, $\theta_{\max}$, that can be achieved by flexing the distal tip of a bronchoscope. The steerable needle is modeled by a minimum radius of curvature r_{curve} and a maximum insertion length l_n.

In this work, we assume the lengths of the stylet and steerable needle are fixed. We define the design $\mathbf{d}$ of a system as a vector consisting of the bronchoscope's radius, the piercing mechanism's maximum actuation angle, and the steerable needle's minimum radius of curvature,

$$\mathbf{d} = \{r_{\mathrm{b}}, \theta_{\max}, r_{\mathrm{curve}}\}. \tag{1}$$

B. Workspace

For a given system design, we evaluate the quality of the design by measuring the reachable workspace as a percentage of the lung volume. We define the set of all reachable configurations given a design $\mathbf{d}$ from a given piercing start pose $p \in SE(3)$ as

$$Q_{\mathbf{d}}(p) = (q_1, q_2, ..., q_n) \tag{2}$$

where $q_i \in SE(3)$ is a configuration of the steerable needle modeled by the pose of its tip. Each $q_i \in Q_{\mathbf{d}}$ is collision-free and is reachable by some collision-free path. The start configuration p is sampled from a set of m piercing start poses, $P_{\mathbf{d}}$, for design $\mathbf{d}$.

We define the set of points in discrete image space that a system design can reach as $W(\mathbf{d}) \subset \mathbb{R}^3$, which consists of all positions in the lung parenchyma that are reachable by the tip of the deployed steerable needle. Since the configurations in $Q_{\mathbf{d}}$ are in a continuous space, we define a function Voxelize() to convert their positional coordinates to discrete image space. This gives us a countable set of voxel coordinates in three-dimensional image space $\{v_1, v_2, ..., v_k\}$, $v_i \in \mathbb{R}^3$ that are accessible via a collision-free path by the system. Formally,

$$W(\mathbf{d}) = \bigcup_{p \in P_{\mathbf{d}}} \text{Voxelize}(Q_{\mathbf{d}}(p)). \tag{3}$$

The total space that is potentially accessible is defined by the voxels inside the lung parenchyma, excluding voxels in O and in the airways. This set of voxels is represented by $V \subset \mathbb{R}^3$. Therefore, the percent of reachable voxels $X_{\mathbf{d}}$ for a specific system design $\mathbf{d}$ is determined by

$$X_{\mathbf{d}} = \frac{|W(\mathbf{d})|}{|V|} * 100. \tag{4}$$

C. Reachable Redundancy

Given the challenging nature of millimeter-level accuracy in piercing during diagnostic bronchoscopy, the more robust a system is to minor changes, the more likely it is that a procedure will be successful. Similar to Burgner-Kahrs et al. [47], we define a notion of reachable redundancy that measures for each voxel the number of unique piercing start configurations from which it is reachable, given a design $\mathbf{d}$. We use this notion to measure the robustness of a design and of lung region access to variability in the piercing start pose. This redundancy is measured by the following equation

$$I_{\mathbf{d}}(x, y, z) = \sum_{p \in P_{\mathbf{d}}} \begin{cases} 1, & \text{if}(x, y, z) \in \text{Voxelize}(Q_{\mathbf{d}}(p)) \\ 0, & \text{otherwise} \end{cases} \tag{5}$$

where $I_{\mathbf{d}}$ is a three-dimensional array with the same dimensions as the CT scan.

IV. Method

In this section, we present our process for determining the reachable workspace given a system design.

A. Lung Anatomy Dataset

To assess the effect of bronchoscope diameter, piercing angle, and needle minimum radius of curvature on the system's reachable workspace, we simulate device deployment in human lungs. We downloaded CT scans from the Lung Image Database Consortium and Image Database Resource Initiative (LIDC-IDRI) image collection [49], [50], a public database for medical image analysis available in The Cancer Imaging Archive (TCIA) [51]. We selected a subset of 35 CT scans with a series identifier of "NLST TLC VOL B30F" due to the stated relationship to the National Lung Screening Trial (NLST) study from 2011 [52]. We excluded scans with poorly visible lung anatomy, and then randomly selected 5 scans from those remaining for inclusion in our study. Table I shows the characteristics of the CT scans.

To identify viable piercing poses and to provide an environment with obstacles for the needle motion planner, we segmented lung anatomy using the method in Fu et al. [53]. The bronchial tree, major blood vessels, and lung pleura were segmented automatically. Lung fissures separating lung lobes were manually segmented in 3D Slicer [54]. We labeled all voxels making up these anatomical tissues and outside of the lung pleural boundary as obstacles in O. Fig. 3 shows an example of the environment with the obstacles.

TABLE I

DATASET CHARACTERISTICS.

LIDC-IDRI Identifier	CT Dimensions (pixels)	Voxel Dimensions (mm)	Voxels in the Lung Parenchyma ($\|V\|$)
LIDC 297	(512, 331, 497)	0.5507 x 0.5507 x 0.7	29,123,470
LIDC 344	(503, 411, 510)	0.6875 x 0.6875 x 0.7	25,123,852
LIDC 487	(376, 420, 512)	0.4609 x 0.4609 x 0.7	28,003,772
LIDC 524	(408, 428, 512)	0.5313 x 0.5313 x 0.7	25,752,601
LIDC 525	(429, 390, 512)	0.5371 x 0.5371 x 0.7	27,423,786

B. Generating Reachable Needle Configurations

Using the motion planner described in [42], we randomly sample m piercing start poses along the airway wall for each system design. This set of piercing start poses is $P_{\mathbf{d}}$. This set represents a subset of all possible piercing poses in the airway that are accessible by a bronchoscope of the specified radius r_{b} and are within the maximum achievable piercing angle $\theta_{\max}$. We determine bronchoscope accessibility by comparing r_{b} with the radius of each airway lumen. Fig. 4 shows the differences between the reach of the three different bronchoscope radii considered.

We evaluate $Q_{\mathbf{d}}$ for all piercing start configuration $p \in P_{\mathbf{d}}$ using the RRT expansion without an explicit goal configuration. We use the RRT-based steerable needle motion planner described in [45]. The motion planner builds a tree in configuration-space from a given start pose where nodes are reachable collision-free end effector poses and edges are collision-free motions between configurations under the kinematic constraints of the needle set by the minimum radius of curvature r_{curve} and insertion length l_n. A needle pose is considered collision-free if it is at least some distance from its nearest-neighbor obstacle voxel. The minimum distance from an obstacle is defined by the radius of a sphere inscribing a voxel, and is determined according to the dimensions of voxels in each CT scan.

Since we expand the RRT without a goal, $Q_{\mathbf{d}}$ is an unordered set of all nodes in the tree, not necessarily any specific motion plan. By not specifying a goal, we allow the algorithm to expand the tree in all possible directions while obeying the kinematic constraints of the system.

The motion planner is implemented using the Motion Planning Templates (MPT) library [55] and Nigh [56], a library for efficient nearest-neighbor search.

Fig. 3. A sample lung environment showing the segmented anatomy that includes the pleural boundary (gray), major blood vessels (red), airway (tan), and lung fissures that separate lung lobes (blue). These serve as obstacles to the motion planner and create a challenging environment where maximizing reachability will depend on the system design.

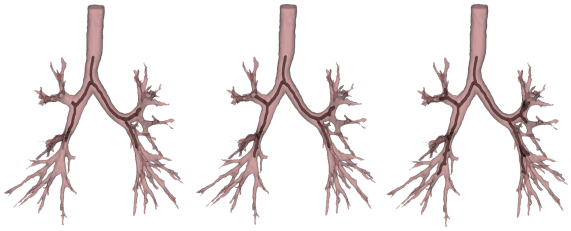

Fig. 4. Effect of bronchoscope diameter on the accessible airway depth (bronchoscope radius, r_{b}, from left to right: 2.5mm, 2.0mm, 1.5mm).

C. Computing Reachable Workspace and Reachable Redundancy

To determine the percentage of the lung, $X_{\mathbf{d}}$, that is reachable for a given design, we first need to calculate $W(\mathbf{d})$ using (3). To do so, we run the needle motion planner for t seconds per piercing pose and record all points in configuration space that are reached in that time. Given the nature of the RRT, we are guaranteed to never over approximate the reachable workspace of the system. Additionally, the RRT expansion asymptotically approaches the true reachable workspace as more time passes.

We convert from continuous configuration space to discrete image space using Voxelize(). This is done by determining which voxel contains the continuous positional coordinate of each needle tip configuration. Thus, we count a voxel as reachable if the RRT expansion by the motion planner reaches a point within that specific voxel. These voxels represent the points in the lung that are reachable via a collision-free path.

We dilate the reachable workspace of the system to approximate 6mm diameter nodules around reachable voxels. The sphere size is motivated by the smallest nodule that is considered clinically significant [57]. The dilation is done in voxel space using a cuboid inscribed by a 6mm diameter sphere centered at the reachable voxel. This voxel neighborhood is appropriately sized with relation to the voxel dimensions of each specific CT scan. For each reachable voxel, we consider its neighboring voxels within this diagnostic region of interest as reached. This reflects the clinical scenario where a successful biopsy need not access the nodule center. This set of reachable dilated voxels is $W(\mathbf{d})$. We determine V by counting voxels within the pleural boundary that are not in O, and then calculate $X_{\mathbf{d}}$ using (4).

We calculate the reachable redundancy of a design $\mathbf{d}$ for a specific voxel v by counting the number of piercing

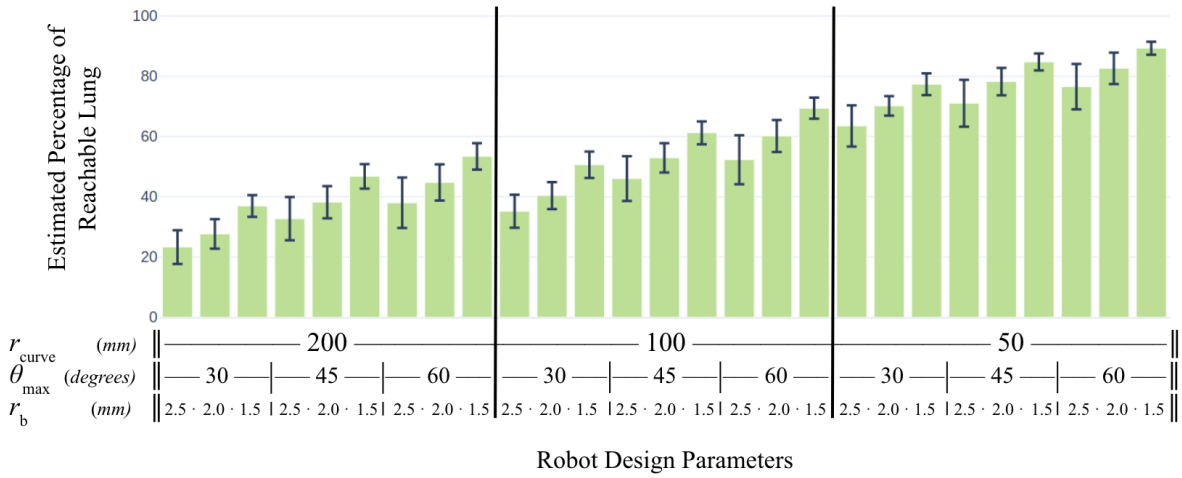

Fig. 5. Estimated percentage of reachable lung for all 27 robot designs, averaged across the five lung environments.

poses whose RRT expansion contains v, as defined in (5). This allows us to define the robustness of a design **d** by evaluating the number of voxels with a redundancy score above a certain threshold. We can also use this redundancy score to identify the robustness of access to specific lung regions under piercing pose variability.

D. Convergence

We performed a convergence analysis on the estimated percentage of the lung that is reachable for a design **d** to determine the values for the number of piercing start configurations, m, and for the time of RRT expansion per start configuration, t. We define convergence as a 1% change or less in the estimated percentage of the lung that is reachable. We increased the number of start configurations by an increment of 1000 and the time allotted to the RRT by an increment of 10 seconds, starting from $m = 1000$ and $t = 10$ seconds, respectively. We determined that $m = 5000$ and $t = 30$ seconds resulted in convergence for both the most constrained and most capable system designs we consider.

V. Results

We evaluate the reachable workspace in 5 human lung environments using all permutations of the following parameter settings: $r_{\mathrm{b}} \in \{2.5\text{mm}, 2.0\text{mm}, 1.5\text{mm}\}$, $\theta_{\max} \in \{30\,\text{degrees}, 45\,\text{degrees}, 60\,\text{degrees}\}$, and $r_{\mathrm{curve}} \in \{200\text{mm}, 100\text{mm}, 50\text{mm}\}$. These values are informed by existing hardware and literature and are meant to capture a wide range of capabilities for the three individual system components. This leads to a total of 27 unique system designs per lung. The stylet maximum insertion length and the needle maximum insertion length are set to 15mm and 135mm, respectively, for all simulations. All experiments were performed on a PC with two 3.4 GHz Intel Xeon E5-1680 processors (16 cores total) with 64GB RAM running Ubuntu 18.04.4.

A. Reachability

The estimated percentage of the lung that is reachable across the 27 different design parameter settings and averaged across the 5 lung environments is shown in Fig. 5. The most capable system design we considered is able to reach approximately 89.3% of the lung volume on average.

In general, as the design becomes more capable (i.e. thinner bronchoscope, greater piercing angle limit, curvier needle), more of the lung becomes reachable. However, the trend is not strictly linear, with some design considerations and trade-offs becoming apparent.

One visible trend is that increased piercing angle capabilities can often overcome limitations in the bronchoscope's diameter. This can be seen when comparing any design with $\{r_{\mathrm{b}} = 2.0\text{mm}, \theta_{\max} = 45\,\text{degrees}\}$ to a design with $\{r_{\mathrm{b}} = 1.5\text{mm}, \theta_{\max} = 30\,\text{degrees}\}$ within the same minimum radius of curvature setting.

Similarly, a decrease in bronchoscope diameter can make up for lower piercing angle capability. This can be seen when comparing a design with $\{r_{\mathrm{b}} = 1.5\text{mm}, \theta_{\max} = 30\,\text{degrees}\}$ to a design with $\{r_{\mathrm{b}} = 2.5\text{mm}, \theta_{\max} = 45\,\text{degrees}\}$ within the same minimum radius of curvature value.

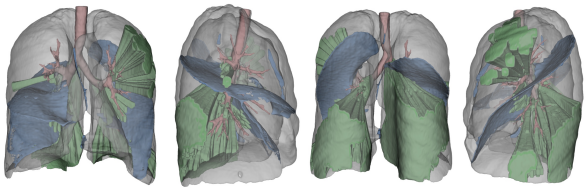

(a) 18.8% of the target space is *reachable* (green) with the most constrained system design $\mathbf{d} = \{r_{\mathrm{b}} = 2.5\text{mm}, \theta_{\max} = 30\,\text{degrees}, r_{\mathrm{curve}} = 200\text{mm}\}$. Uncolored regions in the lung are *unreachable* (81.2%).

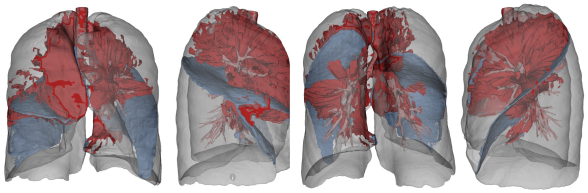

(b) 15.8% of the target space is *unreachable* (red) with the most capable system design $\mathbf{d} = \{r_{\mathrm{b}} = 1.5\text{mm}, \theta_{\max} = 60\,\text{degrees}, r_{\mathrm{curve}} = 50\text{mm}\}$. Uncolored regions in the lung are *reachable* (84.2%).

Fig. 6. Visualization of the reachable and unreachable workspace of two system designs.

Another way to visualize the results of the reachable workspace analysis is to generate 3D representations of the segmented anatomy and color each voxel based on the system's ability to reach it or not. This helps identify the specific regions of the lung that are reachable, and also the regions that remain challenging to reach for even the most capable systems.

Fig. 6a shows the reachable workspace of the most constrained design $\{r_{\mathrm{b}} = 2.5\mathrm{mm}, \theta_{\max} = 30\,\mathrm{degrees}, r_{\mathrm{curve}} = 200\mathrm{mm}\}$ while Fig. 6b shows the *unreachable space* of the most capable design $\{r_{\mathrm{b}} = 1.5\mathrm{mm}, \theta_{\max} = 60\,\mathrm{degrees}, r_{\mathrm{curve}} = 50\mathrm{mm}\}$ in our analysis. The uncolored space in the lung parenchyma represents the *unreachable space* and *reachable space* for the two designs, respectively. Fig. 1 shows both the *reachable* and *unreachable* regions together. These results show that posterior and inferior regions are easily accessible, and that increased device capabilities allow for more comprehensive reach of these regions in addition to access to the middle lung lobe. However, the upper lobes, where a majority of lesions present in patients, are challenging to reach even for the most capable design.

Ideally, we would want 100% of the lung to be reachable. However, analyzing specific lung region access could be used to visualize a given system design's reach on a per-patient basis and determine if a target lesion falls within this space.

The above results included the dilation using 6mm diameter spheres around each reachable voxel, as described earlier. When we loosen this restriction to consider lesions that are 10mm in diameter, we see approximately 93% reachability on average across the five lung environments for the system design $\{r_{\mathrm{b}} = 1.5\mathrm{mm}, \theta_{\max} = 60\,\mathrm{degrees}, r_{\mathrm{curve}} = 50\mathrm{mm}\}$.

B. Redundancy

The reachable redundancy metric serves as a way to measure the robustness of a design and of access to specific lung regions given piercing pose variability. As formalized earlier, we assign every voxel in the reachable lung space a value corresponding to the number of piercing start poses that are able to reach it using a specific system design.

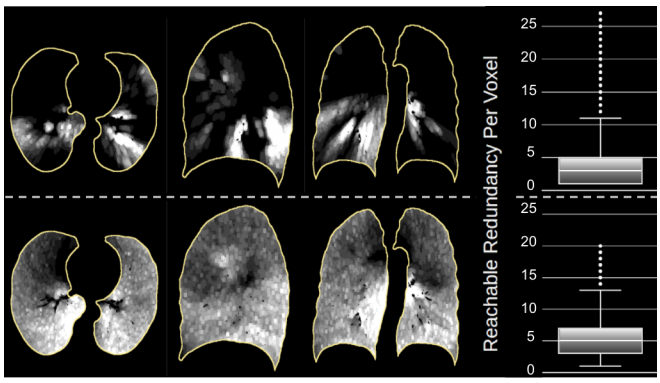

Fig. 7. A visual representation of the reachable redundancy metric on scan LIDC525 for the most constrained system design (top row) and most capable system design (bottom row). White indicates higher reachable redundancy score on a per-design basis.

Fig. 7 shows a visual depiction of the reachable redundancy on scan LIDC525 after the dilation for 6mm diameter nodules. The whiter the voxel the higher the reachable redundancy values, with black indicating zero reach per voxel. The top row represents the reachable redundancy for the most constrained system design, $\{r_{\mathrm{b}} = 2.5\mathrm{mm}, \theta_{\max} = 30\,\mathrm{degrees}, r_{\mathrm{curve}} = 200\mathrm{mm}\}$, and the bottom row represents the reachable redundancy for the most capable system design, $\{r_{\mathrm{b}} = 1.5\mathrm{mm}, \theta_{\max} = 60\,\mathrm{degrees}, r_{\mathrm{curve}} = 50\mathrm{mm}\}$. The constrained design has a higher maximum redundancy count because it explores less of the workspace and therefore repeatedly reaches the same confined regions. The three slices from left to right show views from the transverse plane, sagittal plane, and coronal plane, respectively. The lung regions that are most robust to variability in the piercing pose are generally in the posterior and inferior regions, while the upper lobes are less robust to piercing variability. This is consistent with the results in Fig. 6a and Fig. 6b.

VI. Conclusion

We presented a method for evaluating the clinical reachable workspace of a bronchoscopically-deployed steerable needle lung biopsy robot. We used Monte Carlo random sampling to capture a large subset of possible piercing sites in the airways, and used an RRT-based motion planner to assess the reachability of several system designs, taking into consideration anatomical obstacles. We introduced a method for specific lung region access evaluation that could be used to visualize a system design's reach on a per-patient basis. We showed that the most capable design we considered (which to our knowledge is not yet feasible in hardware) is able to reach approximately 89.3% of the lung parenchyma on average when considering 6mm diameter nodules, and 93% when considering 10mm diameter nodules.

We showed that the upper lung lobe regions, which are known to be challenging to reach and are the site of roughly 60% of lung cancer presentations, remain the most challenging to reach for the system we considered. These findings show that novel approaches may be necessary to address these limitations. Coupling commercial robotic systems that have shown improved reach in these regions [58], [59] with enhanced puncturing mechanisms and curvier needles may be a worthwhile effort.

These results provide insight into the trade-offs and importance of several device parameters. For example, it appears that increased piercing angle capabilities are more meaningful for overall reach than a thinner bronchoscope.

In the future, we plan to perform this analysis in simulation with varying needle length values and in lung phantom models with a real bronchoscopic system. We plan to assess the fidelity of our simulated results when compared to the experimental results where effects like tissue deformation or shearing could play an important role in limiting reachability. We also plan to model more of the system parameters, such as bronchoscope maneuverability, so as to better reflect clinical capabilities.

REFERENCES

[1] P. J. Swaney, A. W. Mahoney, B. I. Hartley, A. A. Remirez, E. Lamers, R. H. Feins, R. Alterovitz, and R. J. Webster III, "Toward transoral peripheral lung access: Combining continuum robots and steerable needles," *Journal of medical robotics research*, vol. 2, no. 01, p. 1750001, 2017.

[2] T. K. Adebar, J. D. Greer, P. F. Laeseke, G. L. Hwang, and A. M. Okamura, "Methods for improving the curvature of steerable needles in biological tissue," *IEEE Transactions on Biomedical Engineering*, vol. 63, no. 6, pp. 1167–1177, 2015.

[3] D. Minhas, J. A. Engh, and C. N. Riviere, "Testing of neurosurgical needle steering via duty-cycled spinning in brain tissue in vitro," in *Annual International Conference of the IEEE Engineering in Medicine and Biology Society*, 2009, pp. 258–261.

[4] W. Street, "Cancer facts & figures 2019," *Am Cancer Soc*, vol. 76, 2019.

[5] J. S. W. Memoli, P. J. Nietert, and G. A. Silvestri, "Meta-analysis of guided bronchoscopy for the evaluation of the pulmonary nodule," *Chest*, vol. 142, no. 2, pp. 385–393, 2012.

[6] D. E. Ost, A. Ernst, X. Lei, K. L. Kovitz, S. Benzaquen, J. Diaz-Mendoza, S. Greenhill, J. Toth, D. Feller-Kopman, J. Puchalski *et al.*, "Diagnostic yield and complications of bronchoscopy for peripheral lung lesions. results of the AQuIRE registry," *American Journal of Respiratory and Critical Care Medicine*, vol. 193, no. 1, pp. 68–77, 2016.

[7] M. Oki, H. Saka, F. Asano, C. Kitagawa, Y. Kogure, A. Tsuzuku, and M. Ando, "Use of an ultrathin vs thin bronchoscope for peripheral pulmonary lesions: a randomized trial," *Chest*, vol. 156, no. 5, pp. 954–964, 2019.

[8] M. M. Wahidi, F. J. Herth, A. Chen, G. Cheng, and L. Yarmus, "State of the art: Interventional pulmonology," *Chest*, vol. 157, no. 3, pp. 724–736, 2020.

[9] M. Rox, M. Emerson, T. E. Ertop, I. Fried, M. Fu, J. Hoelscher, A. Kuntz, J. Granna, J. Mitchell, M. Lester, F. Maldonado, E. A. Gillaspie, J. A. Akulian, R. Alterovitz, and R. J. Webster III, "Decoupling Steerability from Diameter: Helical Dovetail Laser Patterning for Steerable Needles," *IEEE Access*, 10/2020 2020.

[10] A. Majewicz, T. R. Wedlick, K. B. Reed, and A. M. Okamura, "Evaluation of robotic needle steering in ex vivo tissue," in *Proc. of the IEEE International Conference on Robotics and Automation*, 2010, pp. 2068–2073.

[11] T. Adebar, J. Greer, P. Laeseke, G. Hwang, and A. Okamura, "Towards robotic needle steering for percutaneous radiofrequency ablation in the liver: Procedure-specific workspace analysis," in *Proc. Hamlyn Symp. Med. Robot.*, 2015, pp. 67–68.

[12] S. M. LaValle, *Planning algorithms*. Cambridge university press, 2006.

[13] R. Konietschke, T. Ortmaier, U. Hagn, G. Hirzinger, and S. Frumento, "Kinematic design optimization of an actuated carrier for the dlr multi-arm surgical system," in *Proc. of the IEEE/RSJ International Conference on Intelligent Robots and Systems*, 2006, pp. 4381–4387.

[14] P. K. Jamwal, S. Xie, and K. C. Aw, "Kinematic design optimization of a parallel ankle rehabilitation robot using modified genetic algorithm," *Robotics and Autonomous Systems*, vol. 57, no. 10, pp. 1018–1027, 2009.

[15] P. K. Jamwal, S. Hussain, and S. Q. Xie, "Three-stage design analysis and multicriteria optimization of a parallel ankle rehabilitation robot using genetic algorithm," *IEEE Transactions on Automation Science and Engineering*, vol. 12, no. 4, pp. 1433–1446, 2014.

[16] X. Zhang and C. A. Nelson, "Kinematic analysis and optimization of a novel robot for surgical tool manipulation," *Journal of Medical Devices*, vol. 2, no. 2, 2008.

[17] E. Courteille, D. Deblaise, and P. Maurine, "Design optimization of a delta-like parallel robot through global stiffness performance evaluation," in *Proc. of the IEEE/RSJ International Conference on Intelligent Robots and Systems*, 2009, pp. 5159–5166.

[18] A. Kuntz, C. Bowen, C. Baykal, A. W. Mahoney, P. L. Anderson, F. Maldonado, R. J. Webster, and R. Alterovitz, "Kinematic design optimization of a parallel surgical robot to maximize anatomical visibility via motion planning," in *Proc. of the IEEE International Conference on Robotics and Automation*, 2018, pp. 926–933.

[19] L. Zhou, Y. Li, and S. Bai, "A human-centered design optimization approach for robotic exoskeletons through biomechanical simulation," *Robotics and Autonomous Systems*, vol. 91, pp. 337–347, 2017.

[20] J. Hiller and H. Lipson, "Automatic design and manufacture of soft robots," *IEEE Transactions on Robotics*, vol. 28, no. 2, pp. 457–466, 2011.

[21] C.-H. Kuo, J. S. Dai, and P. Dasgupta, "Kinematic design considerations for minimally invasive surgical robots: an overview," *The International Journal of Medical Robotics and Computer Assisted Surgery*, vol. 8, no. 2, pp. 127–145, 2012.

[22] T. Anor, J. R. Madsen, and P. Dupont, "Algorithms for design of continuum robots using the concentric tubes approach: A neurosurgical example," in *Proc. of the IEEE International Conference on Robotics and Automation*, 2011, pp. 667–673.

[23] L. G. Torres, R. J. Webster, and R. Alterovitz, "Task-oriented design of concentric tube robots using mechanics-based models," in *Proc. of the IEEE/RSJ International Conference on Intelligent Robots and Systems*, 2012, pp. 4449–4455.

[24] C. Bedell, J. Lock, A. Gosline, and P. E. Dupont, "Design optimization of concentric tube robots based on task and anatomical constraints," in *Proc. of the IEEE International Conference on Robotics and Automation*, 2011, pp. 398–403.

[25] J. Burgner, H. B. Gilbert, and R. J. Webster, "On the computational design of concentric tube robots: Incorporating volume-based objectives," in *Proc. of the IEEE International Conference on Robotics and Automation*, 2013, pp. 1193–1198.

[26] C. Bergeles, A. H. Gosline, N. V. Vasilyev, P. J. Codd, J. Pedro, and P. E. Dupont, "Concentric tube robot design and optimization based on task and anatomical constraints," *IEEE Transactions on Robotics*, vol. 31, no. 1, pp. 67–84, 2015.

[27] C. Baykal, L. G. Torres, and R. Alterovitz, "Optimizing design parameters for sets of concentric tube robots using sampling-based motion planning," in *Proc. of the IEEE/RSJ International Conference on Intelligent Robots and Systems*, 2015, pp. 4381–4387.

[28] C. Baykal, C. Bowen, and R. Alterovitz, "Asymptotically optimal kinematic design of robots using motion planning," *Autonomous robots*, vol. 43, no. 2, pp. 345–357, 2019.

[29] L. Ingber, "Very fast simulated re-annealing," *Mathematical and computer modelling*, vol. 12, no. 8, pp. 967–973, 1989.

[30] T. K. Morimoto, J. D. Greer, M. H. Hsieh, and A. M. Okamura, "Surgeon design interface for patient-specific concentric tube robots," in *Proc. of the IEEE International Conference on Biomedical Robotics and Biomechatronics*, 2016, pp. 41–48.

[31] N. Abolhassani, R. Patel, and M. Moallem, "Needle insertion into soft tissue: A survey," *Medical engineering & physics*, vol. 29, no. 4, pp. 413–431, 2007.

[32] K. B. Reed, A. Majewicz, V. Kallem, R. Alterovitz, K. Goldberg, N. J. Cowan, and A. M. Okamura, "Robot-assisted needle steering," *IEEE robotics & automation magazine*, vol. 18, no. 4, pp. 35–46, 2011.

[33] A. Favaro, R. Secoli, F. R. y Baena, and E. De Momi, "Model-based robust pose estimation for a multi-segment, programmable bevel-tip steerable needle," *IEEE Robotics and Automation Letters*, vol. 5, no. 4, pp. 6780–6787, 2020.

[34] R. Alterovitz, K. Goldberg, and A. Okamura, "Planning for steerable bevel-tip needle insertion through 2d soft tissue with obstacles," in *Proc. of the IEEE International Conference on Robotics and Automation*, 2005, pp. 1640–1645.

[35] V. Duindam, J. Xu, R. Alterovitz, S. Sastry, and K. Goldberg, "Three-dimensional motion planning algorithms for steerable needles using inverse kinematics," *The International Journal of Robotics Research*, vol. 29, no. 7, pp. 789–800, 2010.

[36] W. Sun, S. Patil, and R. Alterovitz, "High-frequency replanning under uncertainty using parallel sampling-based motion planning," *IEEE Transactions on Robotics*, vol. 31, no. 1, pp. 104–116, 2015.

[37] M. Bernardes, B. V. Adorno, P. Poignet, and G. Borges, "Robot-assisted automatic insertion of steerable needles with closed-loop imaging feedback and intraoperative trajectory replanning," *Mechatronics*, vol. 23, no. 6, pp. 630–645, 2013.

[38] M. C. Bernardes, B. V. Adorno, G. A. Borges, and P. Poignet, "3d robust online motion planning for steerable needles in dynamic workspaces using duty-cycled rotation," *Journal of Control, Automation and Electrical Systems*, vol. 25, no. 2, pp. 216–227, 2014.

[39] R. Alterovitz, M. Branicky, and K. Goldberg, "Motion planning under uncertainty for image-guided medical needle steering," *The International journal of robotics research*, vol. 27, no. 11-12, pp. 1361–1374, 2008.

[40] J. Van Den Berg, S. Patil, R. Alterovitz, P. Abbeel, and K. Goldberg, "Lqg-based planning, sensing, and control of steerable needles," in

Algorithmic Foundations of Robotics IX. Springer, 2010, pp. 373–389.

[41] J. Xu, V. Duindam, R. Alterovitz, and K. Goldberg, "Motion planning for steerable needles in 3d environments with obstacles using rapidly-exploring random trees and backchaining," in *IEEE International Conference on Automation Science and Engineering*, 2008, pp. 41–46.

[42] A. Kuntz, L. G. Torres, R. H. Feins, R. J. Webster, and R. Alterovitz, "Motion planning for a three-stage multilumen transoral lung access system," in *Proc. of the IEEE/RSJ International Conference on Intelligent Robots and Systems*, 2015, pp. 3255–3261.

[43] F. Liu, A. Garriga-Casanovas, R. Secoli, and F. Rodriguez y Baena, "Fast and adaptive fractal tree-based path planning for programmable bevel tip steerable needles," *IEEE Robotics and Automation Letters*, vol. 1, no. 2, pp. 601–608, 2016.

[44] M. Pinzi, S. Galvan, and F. R. y Baena, "The adaptive hermite fractal tree (AHFT): a novel surgical 3d path planning approach with curvature and heading constraints," *International journal of computer assisted radiology and surgery*, vol. 14, no. 4, pp. 659–670, 2019.

[45] S. Patil and R. Alterovitz, "Interactive motion planning for steerable needles in 3d environments with obstacles," in *IEEE RAS & EMBS International Conference on Biomedical Robotics and Biomechatronics*, 2010, pp. 893–899.

[46] F. Zacharias, C. Borst, and G. Hirzinger, "Capturing robot workspace structure: representing robot capabilities," in *Proc. of the IEEE/RSJ International Conference on Intelligent Robots and Systems*, 2017, pp. 3229–3236.

[47] J. Burgner-Kahrs, H. B. Gilbert, J. Granna, P. J. Swaney, and R. J. Webster, "Workspace characterization for concentric tube continuum robots," in *Proc. of the IEEE/RSJ International Conference on Intelligent Robots and Systems*, 2014, pp. 1269–1275.

[48] Y. Cao, K. Lu, X. Li, and Y. Zang, "Accurate numerical methods for computing 2d and 3d robot workspace," *International Journal of Advanced Robotic Systems*, vol. 8, no. 6, p. 76, 2011.

[49] S. G. Armato III, G. McLennan, L. Bidaut, M. F. McNitt-Gray, C. R. Meyer, A. P. Reeves, B. Zhao, D. R. Aberle, C. I. Henschke, E. A. Hoffman *et al.*, "The lung image database consortium (LIDC) and image database resource initiative (IDRI): a completed reference database of lung nodules on ct scans," *Medical physics*, vol. 38, no. 2, pp. 915–931, 2011.

[50] ——, "Data from lidc-idri," *The Cancer Imaging Archive*, 2015.

[51] K. Clark, B. Vendt, K. Smith, J. Freymann, J. Kirby, P. Koppel, S. Moore, S. Phillips, D. Maffitt, M. Pringle *et al.*, "The cancer imaging archive (TCIA): maintaining and operating a public information repository," *Journal of digital imaging*, vol. 26, no. 6, pp. 1045–1057, 2013.

[52] N. L. S. T. R. Team, "Reduced lung-cancer mortality with low-dose computed tomographic screening," *New England Journal of Medicine*, vol. 365, no. 5, pp. 395–409, 2011.

[53] M. Fu, A. Kuntz, R. J. Webster, and R. Alterovitz, "Safe motion planning for steerable needles using cost maps automatically extracted from pulmonary images," in *Proc. of the IEEE/RSJ International Conference on Intelligent Robots and Systems*, 2018, pp. 4942–4949.

[54] A. Fedorov, R. Beichel, J. Kalpathy-Cramer, J. Finet, J.-C. Fillion-Robin, S. Pujol, C. Bauer, D. Jennings, F. Fennessy, M. Sonka *et al.*, "3d slicer as an image computing platform for the quantitative imaging network," *Magnetic resonance imaging*, vol. 30, no. 9, pp. 1323–1341, 2012.

[55] J. Ichnowski and R. Alterovitz, "Motion planning templates: A motion planning framework for robots with low-power cpus," in *Proc. of the IEEE International Conference on Robotics and Automation*, 2019, pp. 612–618.

[56] ——, "Concurrent nearest-neighbor searching for parallel sampling-based motion planning in so (3), se (3), and euclidean spaces," in *International Workshop on the Algorithmic Foundations of Robotics*. Springer, 2018, pp. 69–85.

[57] I. J. Anderson and A. M. Davis, "Incidental pulmonary nodules detected on ct images," *Jama*, vol. 320, no. 21, pp. 2260–2261, 2018.

[58] A. C. Chen and C. T. Gillespie, "Robotic endoscopic airway challenge: Reach assessment," *The Annals of thoracic surgery*, vol. 106, no. 1, pp. 293–297, 2018.

[59] D. I. Fielding, F. Bashirzadeh, J. H. Son, M. Todman, A. Chin, L. Tan, K. Steinke, M. N. Windsor, and A. W. Sung, "First human use of a new robotic-assisted fiber optic sensing navigation system for small peripheral pulmonary nodules," *Respiration*, vol. 98, no. 2, pp. 142–150, 2019.